Nuclear physics using ultrafast high-power laser ion acceleration

Mark Yuly, Andrew Bo, Avery Belanger, Owen Fall, Stephen Padalino, Charlie Freeman.

I. Ultrafast high-power lasers as a tool for nuclear science

Ultrafast high-power lasers provide a new tool for the study of nuclear science by producing large numbers of energetic ions in a single burst. This can be carried out using inertial confinement fusion (ICF) or laser ion acceleration methods such as target normal sheath accelerations (TNSA) at facilities such as the Laboratory for Laser Energetics (LLE) and the National Ignition Facility (NIF).

In ICF a ponderable mass of nuclear fuel is raised to a high enough temperature (several keV) and held at that temperature long enough for a significant fraction of the reactant nuclei to undergo a nuclear reaction. Because this is the case, even reactions with extremely small cross sections will occur in detectible numbers. To give an idea of the scale, consider NIF shot N221204, widely believed to be the first time ignition was achieved by every definition. In this shot, approximately 200 μg of fuel were imploded, resulting in a hot-spot mass of approximately 20 μg [1,2] with a fuel burn fraction of 4.33% giving a total DT neutron yield of about 10^{18} [3]. Even for deuteron or triton-initiated reactions with 10^{-7} times the DT cross section, doping the target to 1% with the desired reactant isotope would still yield 10^{9} reactions, which, if the product nuclei are radioactive, could be easily measurable by counting the product decays in the relatively quiet environment milliseconds or even seconds after the shot.

For TNSA induced reactions the number of energetic deuterons or tritons is less than the 10^{18} reached using ICF, but a recent experiment [4] using the OMEGA-EP laser generated as many as 10^{12}, focused into a beam with much higher energies, reaching up to as high as about 15 MeV. Since for most reactions the cross section is larger at these energies, similar numbers of product nuclei to ICF can still be obtained using TNSA.

For nuclear activation type measurements, the fact that these energetic ions are all produced within a fraction of a nanosecond has tremendous advantages over using a particle accelerator to produce the ions. Figure 1 shows a representative example of the two techniques.

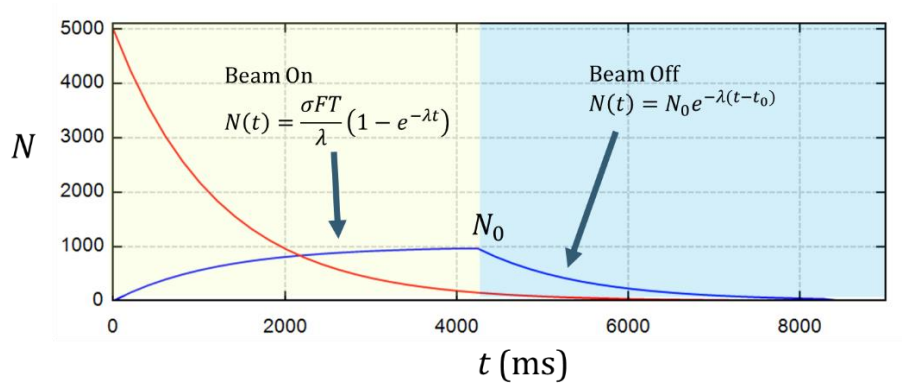

Figure 1. The number of product nuclei (N) as a function of time (t) for a representative activation measurement illustrating the difference between using an accelerator (blue curve) and ICF or TNSA (red curve). For the accelerator experiment, the beam first hits the target creating reaction products (yellow shaded) eventually equilibrium is reached (N_0) where the rate of creation equals the rate of decay, then the beam is turned off and the reaction products decay and are counted (blue shaded). For the laser-driven experiment, all of the product nuclei are created so quickly that essentially none can decay until after the laser pulse.

For the traditional accelerator-based activation experiment, the beam strikes the target over a period of time, during which the number of reaction products (N) builds up and, if they are radioactive, also decays, according to the relationship

$$N(t) = \frac{\sigma F T}{\lambda}\left(1 - e^{-\lambda t}\right) \tag{1}$$

where σ is the reaction cross section (cm^2), F is the number current of the beam (s^{-1}), T is the areal number density (nuclei/area) of the target, λ is the decay constant (s^{-1}), and t is the time (s). The decay constant is related to the half-life by $t_{1/2} = \ln 2/\lambda$. Clearly, equilibrium (N_0) is approached as the rate products are decaying approaches the rate they are produced

$$N_0 = \frac{\sigma F T}{\lambda}. \tag{2}$$

After the beam is turned off, the product nuclei decay according to

$$N(t) = N_0 e^{-\lambda t} \tag{3}$$

where in this case t is the time since the beam ended.

On the other hand, in the laser-driven experiment all of the nuclear reactions occur in a fraction of a nanosecond, so fast that essentially none of the product nuclei can decay during the period when they are being created. This leads to a larger N_0 for a given number of incident ions. Moreover, because the number of product nuclei reaches a maximum value at equilibrium, in the accelerator experiment the beam must be pulsed in order to reach the same number product nuclei as a single pulse in the laser-driven experiment. All of these short pulses must be followed by a counting period, resulting in a much longer experiment with a much larger number of background counts. These problems with the accelerator-type experiment become more pronounced for very small cross sections and very short half-lives.

On a more practical level, these laser-driven approaches have the advantage of being able to initiate tritium-induced reactions, which may be especially important in understanding how nucleosynthesis occurs in core collapse supernovae, big bang models, and neutron star mergers. Moreover, tritium neutron transfer reactions, if they were measured, would provide additional tests of ab-initio neutron-rich nuclear structure models that have only recently been developed. Unfortunately, very few tritium-induced reactions have been studied in the past because of the radiological hazards involved in accelerating tritons and the possibility of contaminating the accelerator beamline. Large laser facilities like the NIF and LLE are already set up to handle tritium, which is confined to target chamber and can be recycled.

The Short-lived Isotope Counting System (SLICS) was developed over the past eight years [5, 6, 7, 8, 9] to detect the radioactive reaction products produced in laser-driven activation experiments involving light ions, of both the ICF and TNSA type. The detector, which consists of a dE-E phoswich plastic scintillator detector and associated high-speed readout electronics, has been tested in a previous OMEGA-60 ride-along experiment [10, 11, 12], in experiments [11, 13] to trap and count radioactive reaction products in a simulated-ICF neutral radioactive expanding gas, and in a TNSA experiment [14, 15] using the Multi-Terawatt laser (MTW) to accelerate deuterons to produce and detect ^{8}Li via the ^{7}Li(d,p)^{8}Li reaction.

The three subsequent sections of this report describe the progress made during the 2023-2024 academic year and summer of 2024, namely, the analysis of the MTW experiment from last summer, an experiment using the SUNY Geneseo tandem Pelletron to test the Geant4 simulation predictions of the beta detection efficiency of SLICS, and a ride-along experiment at LLE to test the ability of SLICS to identify and count short-lived isotopes outside the OMEGA-60 target chamber milliseconds after a high-yield DT shot.

II. Results of MTW test of SLICS detector system using TNSA deuterons (July 2023)

An experiment to test the ability of the SLICS detector to detect short-lived product nuclei from light ion reactions initiated by TNSA-accelerated deuterons was carried out using the MTW laser during the summer of 2023. This experiment, the purpose of which was simply to use the ^{7}Li(d,p)^{8}Li reaction to test whether the detector could be used in this way, exceeded expectations by giving such clean beta decay curves that it was possible to measure the yield. Unfortunately, other aspects of the experiment, such as not accurately knowing the detector efficiency, target thickness or deuteron energy distribution, made it difficult to predict the theoretical yield for comparison.

The setup of this experiment was described in detail elsewhere [14, 15], so it will only be briefly summarized here. As shown in Figure 2, MTW laser pulses (~13-19 J, 11-14 ps) struck a 0.25 mm^2 deuterated polyethylene (CD2) target, ejecting TNSA deuterons that hit a thin natural Li target film on a 25 μm thick stainless-steel substrate, causing the ^{7}Li(d,p)^{8}Li reaction. The CD2 laser target was aligned so that the surface normal pointed at the Li nuclear target. The SLICS phoswich scintillator, light guide, and photomultiplier tube were placed immediately downstream the Li target, and a CAEN N6730SB Digitizer was used to count the 840 ms half-life beta decay of the ^{8}Li, beginning a few milliseconds after the laser shot. The SLICS phoswich detector consisted of a fast thin and slow thick scintillator sandwiched together to allow incident particles to be identified by their different rates of energy loss. Incident deuteron energy spectra were measured using time-of-flight (TOF) to a small scintillator in front of the Li target and, for comparison, with a Thompson parabola spectrometer.

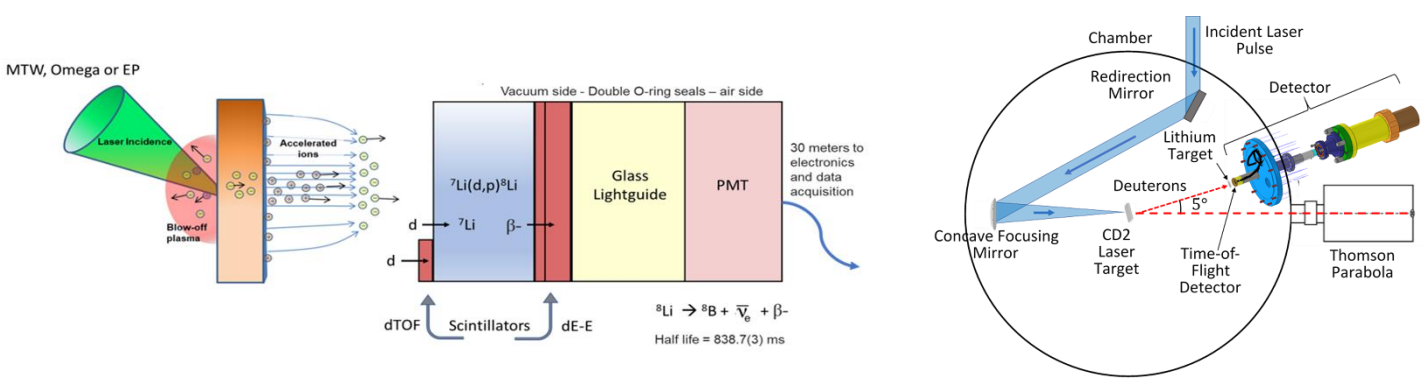

Figure 2. Overview of the MTW experiment. (Left) Conceptual diagram. A high-power short laser pulse from MTW struck a deuterated polyethylene target, blowing the electrons off the opposite surface. This created a strong electric field that accelerated protons and deuterons toward the natural lithium target. Some of these ions hit the time-of-flight scintillator allowing the energy spectrum to be measured. In the lithium target, deuterons caused the ^{7}Li(d,p)^{8}Li reaction to occur, the subsequent ^{8}Li beta decays were counted by the dE-E phoswich detector. (Right) Physical layout. The laser pulse enters the MTW target chamber and is directed to and focused onto the deuterated polyethylene laser target. Deuterons leaving the laser target strike the natural lithium nuclear target just upstream of the SLICS detector. The Thomson parabola allows the deuteron energy spectrum to be measured, albeit at a different angle.

The Li nuclear targets were created by physical vapor deposition as described in Ref. [14, 16]. Because of the need to open the MTW target chamber to replace the laser targets, the lithium nuclear targets were necessarily exposed to air. The original hope was that a thin protective coating of tin or polyethylene could be deposited over the lithium, but that was not ready in time. Therefore, the lithium targets used in the experiment were heavily oxidized, consisting of an unknown mixture of different lithium compounds, most likely lithium hydroxide, lithium oxide and lithium nitride.

The lithium film thicknesses were measured before they oxidized, shortly after removal from the deposition chamber in an argon-filled glove box, using a Mitutoyo IP54 mechanical micrometer. They were then stored in air, and the oxidized film thicknesses were measured using Rutherford Backscattering and by counting the alpha particles produced in the $^{7}Li(p,\alpha)^{4}He$ reaction with the tandem Pelletron at SUNY Geneseo. Figure 3 shows the areal densities measured this way versus the areal densities of the pure lithium metal film measured using the micrometer. While there is a linear relationship as expected, the micrometer-measured thickness is approximately a factor of two larger. This may be a result of oxides already starting to form for the micrometer thickness measurement, making the physical thickness of the film greater for the same amount of lithium.

Ultimately, this meant that although the ^{7}Li areal density was known from the accelerator measurements, the deuteron energy loss, which depended on the composition of the lithium compounds formed, was unknown. In the following analysis, this energy loss was not accounted for, even though it is clear it will significantly affect the shape of the deuteron energy spectrum as the deuterons pass though the target. Also, the target thickness is only known as well as the underlying $^{7}Li(p,\alpha)^{4}He$ cross section, which is somewhat controversial since the JENDL 4.0 and ENDF/B-VIII.0 evaluated cross section databases disagree by a factor of two [17].

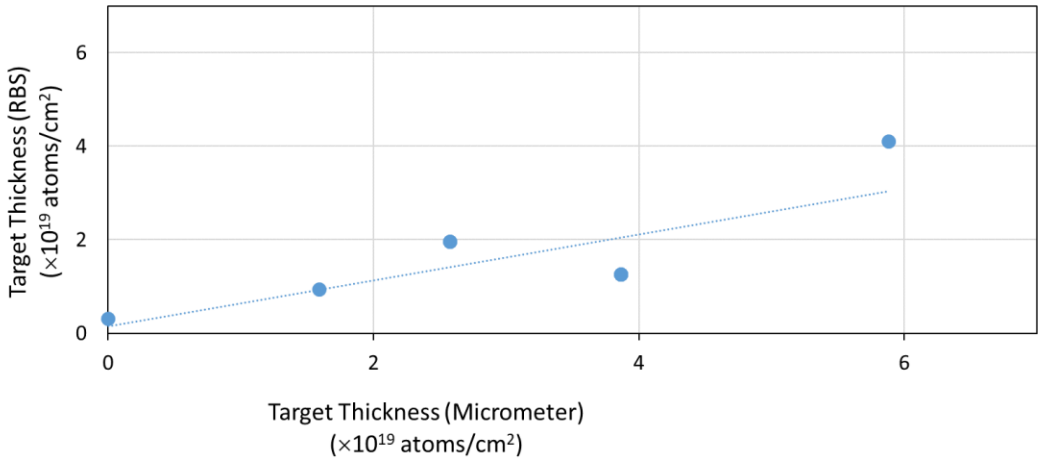

Figure 3. RBS vs. micrometer areal density corresponding to pure lithium of the measured thickness. While there is a linear relationship, the micrometer-measured thickness is approximately a factor of two larger.

In order to measure the ^{8}Li yield, the number of ^{8}Li beta decays was counted as a function of time using the SLICS detector. As was described in Refs. [14, 15], events falling into the region of the 2D dE-E histogram corresponding to beta particles were selected, as shown in Figure 4. The number of beta events and the integral of the number of beta events were histogrammed as a function of time, as shown in Figure 5, to give the decay and growth curves, respectively.

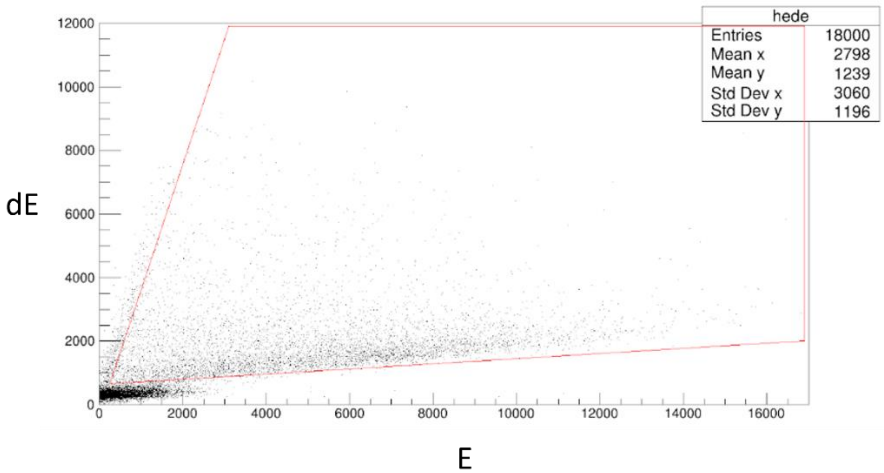

Figure 4. Two-dimensional histogram of dE vs. E pulse heights for MTW shot 15978. The density of dots represents the number of beta events in the energy bin. Events inside the red quadrilateral are counted as beta particles.

Each growth curve was fit with Equation (4), which is the integral of the exponential decay curve, Equation (3), plus the integral of a constant background rate, B,

$$N(t) = N_0'\left(1 - e^{-\lambda t}\right) + Bt. \tag{4}$$

Immediately after the laser shot, the count rate was very high, presumable due to the electronic noise which could be seen with an oscilloscope. It is believed this noise may have originated in the laser amplifiers. For this reason, the fit began typically with $t = 0$ at 200 ms after the laser shot, then the number N_0 that would be detected starting immediately after the laser shot was calculated using the exponential correction factor $N_0 = N_0' e^{\lambda(200\text{ ms})}$. The decay constant of ^{8}Li was fixed to the previously measured value $\lambda = 0.82645\text{ s}^{-1}$.

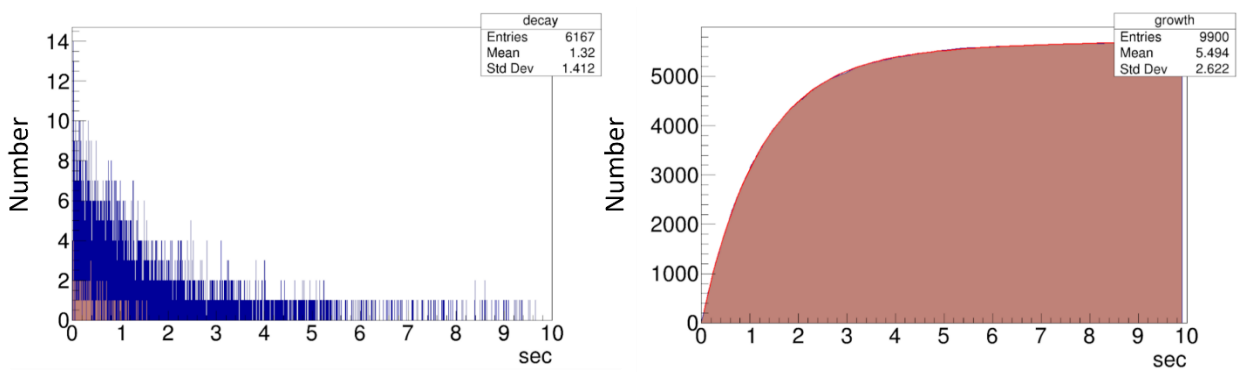

Figure 5. Decay and growth curve for MTW shot 15978. The decay curve (left) shows the number of counts in each 1 ms wide time bin. The growth curve (right), which is the integral of the number of decays, was fit (red curve) with Equation (4) to determine the ^{8}Li yield.

The number of detected ^{8}Li beta decays, N_0, was less that the total yield of ^{8}Li nuclei created since not all beta particles entered the detector and fell inside the selection region in the 2D dE-E histogram. A Geant4 simulation [15] of the SLICS detector was employed to estimate the efficiency to be $e = 45.61\%$ for the 1.14 cm radius lithium films employed in this experiment, which is not far from the naïve expectation of $e = 50\%$ from just considering the solid angle. The yield was then calculated using $Y = N_0/e$. Table 1 shows the best fit results.

Table 1. Growth curve values (N_0', B) and uncertainties ($\delta N_0'$, δB) fit using MINUIT, and the resulting ^{8}Li yield (Y).

MTW Shot	N_0'	$\delta N_0'$	B	δB	Y
15975	3559	1.65	25.63	0.27	9331
15976	2064	1.25	4.70	0.21	5412
15978	5509	2.03	20.64	0.33	13297
15984	2000	1.23	7.96	0.20	5244
15988	3144	1.69	44.84	0.30	15965
15990	2486	1.41	33.74	0.24	7078
15991	4677	1.90	29.09	0.32	12778

The Thomson parabola was used to identify and measure the energy spectrum of the ions that entered it. Unfortunately, it could not be placed at the same angle relative to the incident laser beam as the nuclear target and SLICS detector, which meant that when the deuteron energy spectrum was measured the CD2 laser target normal either had to point at the Thomson parabola, which meant the beam spot was smaller than for the SLICS measurements, or it had to point at the Li nuclear target, which meant the Thomson parabola was measuring the deuteron spectrum 5° away from the center of the deuteron beam. As is clear from Figure 6, which shows the measured energy spectrum for four separate laser shots with different targets and angles, the deuteron energy spectrum depended strongly on the angle. When the laser struck the polyethylene laser target at an angle, the beam spot was larger than when it was normal, resulting in more low energy and fewer high energy deuterons. The laser shots with the non-deuterated polyethylene targets show essentially no deuterons, the peak at low energies gives an indication of the Thomson parabola ability to resolve the H+ and D+ bands at low energy.

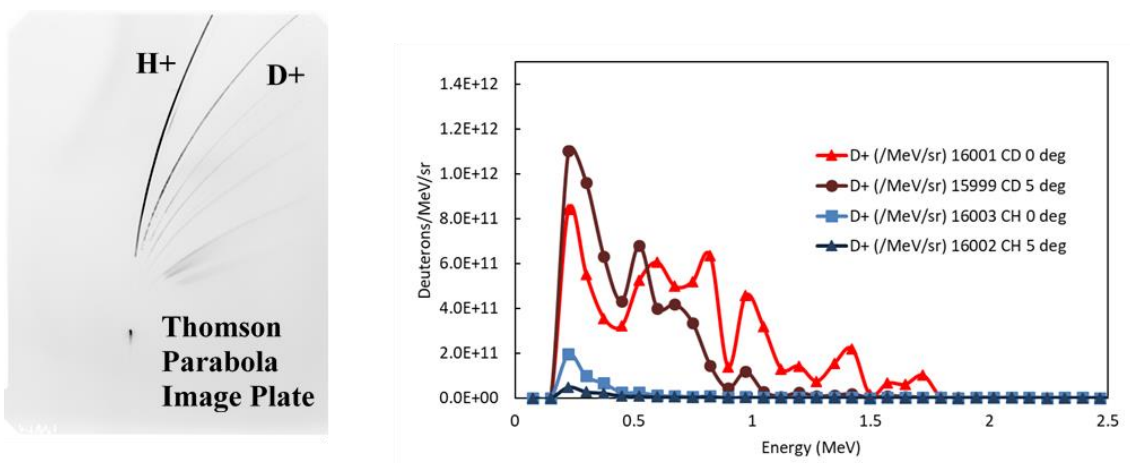

Figure 6. (Left) Thomson Parabola Spectrometer image plate. Parallel electric and magnetic fields in the spectrometer separated ions by mass and energy. Protons and deuterons from the deuterated polyethylene target traveled through a pinhole and were deflected into bands. (Right) Deuteron energy spectra from the deuterated polyethylene targets at 0° (brown) and 5° (red), and non-deuterated polyethylene targets at 0° (light blue) and 5° (dark blue).

In Figure 7 the measured yields are compared with the yields predicted by the convolution of the cross section and the deuteron energy distribution as measured with the Thomson Parabola given by

$$Y = \int_{0\ \mathrm{MeV}}^{2.5\ \mathrm{MeV}} D(E) \cdot T \cdot \Omega \cdot \sigma(E)\, dE, \tag{5}$$

where $D(E)$ is the energy spectrum (deuterons/MeV/sr) of the deuterons incident on the lithium target as measured by the Thomson parabola, T is the areal number density of lithium on the target (^{7}Li/cm^2) as determined using the ^{7}Li(p,α)^{4}He measurement, Ω is the solid angle of the detector (sr), and $\sigma(E)$ is the cross section of the reaction ^{7}Li(d,p)^{8}Li (cm^2). No attempt was made to correct for the energy loss of the deuterons in the target.

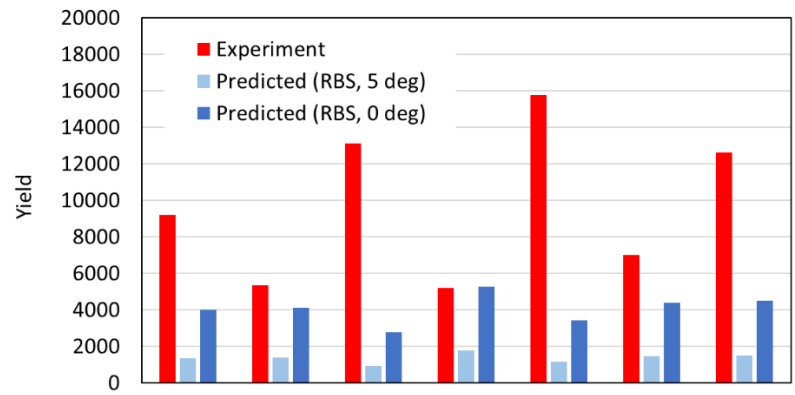

MTW Shot Number	15975	15976	15978	15984	15988	15990	15991
LI Thickness (10^{19} ^{7}Li/cm^2)	2.57	2.57	3.86	5.88	1.59	3.86	3.86
Laser Energy (J)	18.6	18.9	19.5	13.5	13.5	13.1	13.3
Target Distance (mm)	375	375	375	375	222	222	222

Figure 7. Comparison of predicted (red) with experimentally measured (blue) ^{8}Li yields for several MTW laser shots with different nuclear target thicknesses, laser energies, and nuclear target distances. Yields were predicted using the measured deuteron energy spectrum obtained with the laser normal to the laser target (dark blue, 0°) and at 5° to the normal (light blue).

The predicted yield was calculated for a distance from the laser to the nuclear target of 375 mm, which was the correct distance for most of the laser shots, but which was changed to 222 mm for some shots toward the end of the experiment. The yields were therefore multiplied by a correction factor to account for the different solid angle. No attempt was made to correct for the angular distribution of the deuteron flux (see Fig. 5 in Ref. 18) which could result in a different deuteron spectrum for different target distances.

Finally, the laser pulse energy and width varied dramatically from shot to shot, from 11.2 to 19.5 J and 11.2 to 13.6 ps. An attempt to correct for the changing laser energy by multiplying by a factor, obtained by fitting a straight line, shown in Figure 8, to the 10 ps data points in Fig. 4 of Ref. 18. This factor represented the ratio of the deuteron yields from Fig. 4 of Ref. 18 for the ^{8}Li producing laser shot to the corresponding Thomson parabola laser shot.

It is clear from Figure 7 that overall the predictions underestimate the actual yield. On the whole the predictions using the deuteron energy spectrum with the laser target normal to the laser beam (0°) agree better than those with the laser target at 5°, but even then they underestimate the yield by as much as almost a factor of five. The fact that the 0° predictions are closer is surprising since the actual measurements were made at 5°. However, the measurements with the laser target at 5° measured the spectrum at 5° and not 0° as in the actual experiment.

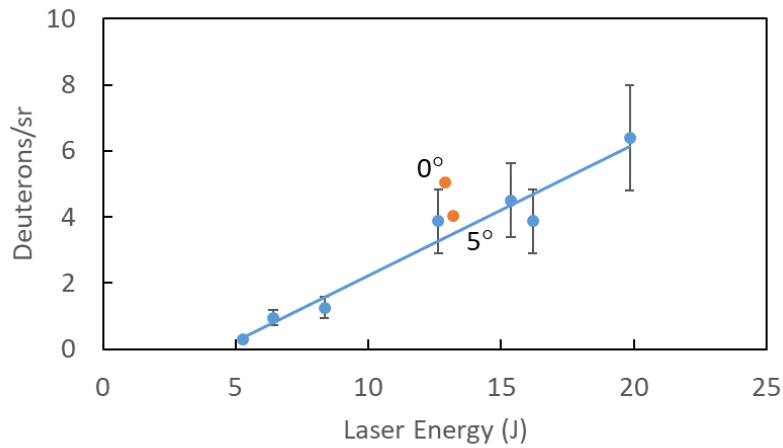

Figure 8. Total deuteron yield as a function of laser energy for approximately 10 ps MTW laser pulses. Data from Fig. 4.11 in Ref. 18 (blue) for deuterated titanium foil targets, the red symbols are from the present experiment using deuterated polyethylene targets at 0° and 5° as described in the text.

It is difficult to see what is causing the disagreement between the measured and predicted yield. In making the predictions of estimated yield, approximate (or even possibly incorrect) values were used in each term of Equation (5):

1. The deuteron energy spectrum *D(E)* was measured with the wrong laser target angle, or the wrong deuteron angle. It is difficult predict the effect of this on the estimated yield. Moreover, the energy loss of the deuterons as they travel through the target was not included in the calculation.
2. The target thickness *T* measured using the ^{7}Li(p,α)^{4}He reaction could change by as much as a factor of two, depending on which evaluated cross section is used.
3. There is disagreement between previous measurements of the ^{7}Li(d,p)^{8}Li total cross section, by as much as a factor of two in the region of interest.
4. The detector efficiency used in determining the experimental yield could be wrong. It was determined using a Geant simulation that did not include many known effects, and recent measurements of the efficiency seem lower.

III. Experimental test of SLICS beta detection efficiency from GEANT simulation (July 2024)

To use the SLICS detector to make cross sections measurements, the absolute efficiency of the detector for detecting beta particles coming from decays on the front of the detector, where the radioactive products are created (TNSA) or captured (ICF), must be known. Just from the geometry it is clear that the efficiency, or the ratio of the number of decays detected to the total number, must be less than 0.5.

The detector efficiency has been estimated using a Geant4 simulation of the detector. This simulation includes the dE and E scintillators and the lithium target and substrate foil. It also can be used to simulate other materials surrounding the detector. It does not account for light lost entering and traveling down the light guide, or for any position sensitivity of the photomultiplier. Each beta particle is tracked as it travels along its path inside the scintillators, and the total energy lost in each scintillator is recorded and used to produce the 2D dE-E histogram. Figure 9 shows an example of a Geant4 simulation, in this case, for a ^{207}Bi point source located at the center of the detector face. The ^{207}Bi emits

monoenergetic electrons in addition to a beta spectrum, and can be used to roughly calibrate the energy scales of the dE and E scintillators.

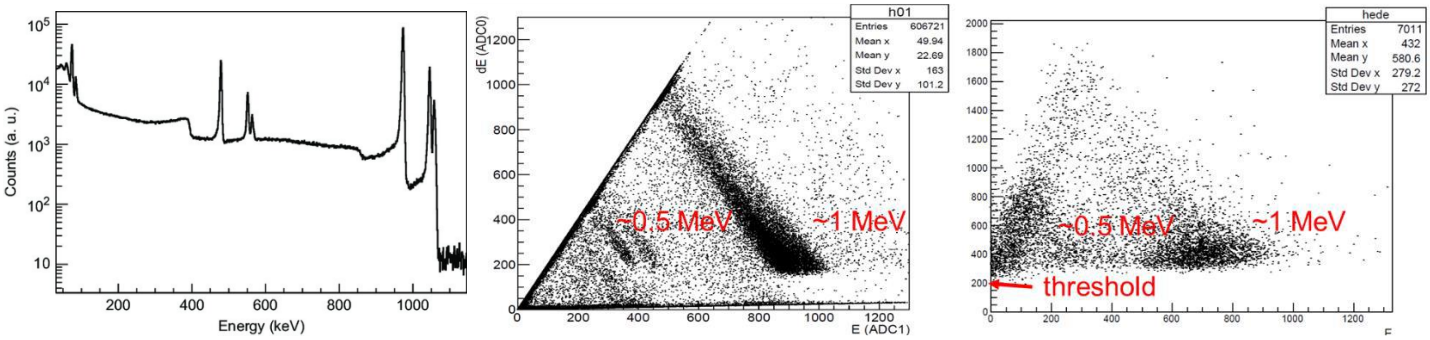

Figure 9. Example of the Geant4 simulation (center) of the 2D dE-E histogram produced by a ^{207}Bi conversion electron source. The ^{207}Bi electron energy spectrum [19] (left) has a broad beta distribution, with monoenergetic electron conversion peaks at 482, 554, 976 and 1048 keV. The 2D histogram measured using the SLICS detector (right) has the same features as the simulation, but they are smeared out

Beta events are selected by counting the number of events in a certain region of the 2D dE-E histogram. To determine the number of product nuclei, the number of detected betas must be divided by the efficiency, i.e. the fraction of the total number that get detected. This number can be predicted by counting the number of simulated events in the same region of the 2D histogram as was used in the experimental measurement. In order to ensure the same region is counted, the ^{207}Bi monoenergetic electron peaks are used to calibrate the dE and E energy scales.

To calculate the efficiency for the MTW experiment described earlier, a ^{8}Li point source was simulated on the front of the SLICS detector at several distances from the center [15]. As shown in Figure 10, the efficiency at each radius was determined, then integrated to get the overall efficiency of the detector for a source of the correct radius covering the front face.

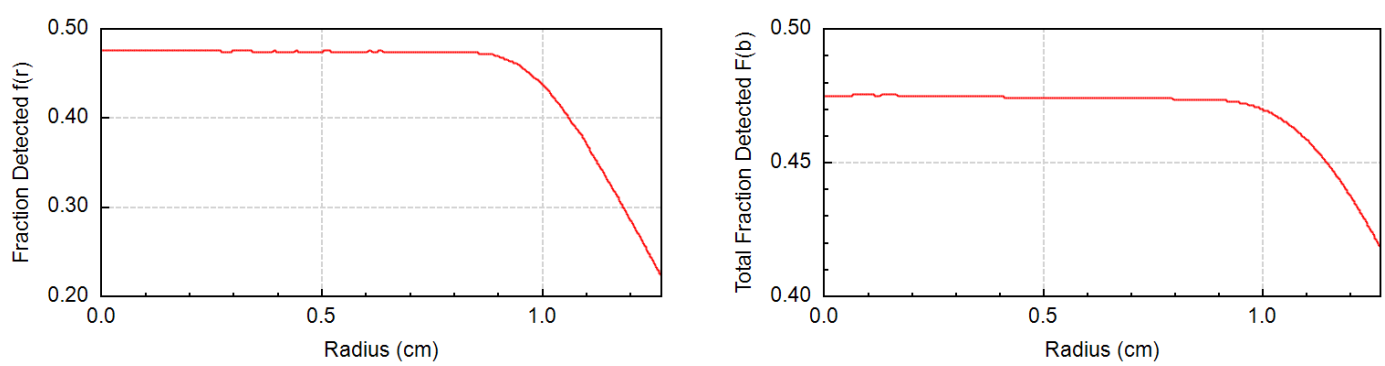

Figure 10. (Left) The fraction of beta particles detected as a function of the radial position of the ^{8}Li point source for the dE-E region used in the MTW experiment (left) was simulated, then used to predict the absolute efficiency as a function of target radius for a 1 inch scintillator (right).

In order to test the ability of the Geant4 simulation to correctly predict the efficiency of the SLICS detector, an experiment was carried out using the SUNY Geneseo 1.7 MV tandem Pelletron accelerator. The experiment, which was carried out by faculty and students from SUNY Geneseo and Houghton University (see Figure 11), used the 30R beamline into which the SLICS detector and two silicon detectors were placed as shown in Figure 12. An approximately 5 nA beam of 1.5 MeV deuterons, with beam a spot approximately 1 mm in diameter, was allowed strike a 1 μm thick, 19 mm diameter natural

lithium film that was on a 25.4 μm thick 304 stainless steel substrate, just upstream of the SLICS detector. The 840 ms half-life beta decays of the ^{8}Li produced by the ^{7}Li(d,p)^{8}Li reaction were counted by the SLICS detector, while the Canberra LEC 500- 3000 500 mm^{2} lithium-compensated silicon detector was used to detect backward scattered alpha particles from the ^{6}Li(d,α)^{4}He reaction.

The preparation of the lithium targets used the deposition process described in Refs. [14, 16]. Prior to placing the target into the front of the detector, it was dipped and then very slowly withdrawn from a beaker of DC 704 diffusion pump oil, creating an approximately 2.2 μm thick film to protect the lithium from the air. The thicknesses of the target layers were measured by counting scattered protons using Rutherford backscattering (RBS) and by counting energetic alpha particles produced by ^{7}Li(p,α)^{4}He. As with the MTW experiment, the accuracy of the Li thickness measurement is limited by the accuracy of the ^{7}Li(p,α)^{4}He cross section used to calculate it.

Figure 11. Houghton students Avery Belanger, Andrew Bo and Owen Fall setting up the 30R scattering chamber at SUNY Geneseo (left) and collecting and analyzing the data at the counting station (center). Houghton and SUNY Geneseo students and faculty in the accelerator control room (right).

The electronics block diagram for SLICS used in this experiment is shown in Figure 13. When the Faraday cup was removed, allowing the deuteron beam to strike the lithium target, the resulting radiation created a high count rate in the NaI detector, causing the output of the NIM latch circuit to latch high. When the cup was reinserted to block the beam, the latch stayed high for a specified amount of time, usually 10 or 11 ms, during which any new detector pulse would reset the latch for another 10 or 11 ms. A C program running on a Raspberry Pi single board computer began looking for the falling edge from the latch circuit, indicating the Faraday cup had been inserted to cut off the beam. When it detected the falling edge, it enabled data collection by the CAEN NB6730SB digitizer, which was controlled and read out by an Atomic Pi single board computer. Both the Atomic Pi and Raspberry Pi were controlled via an ethernet remote session.

A 30-gauge 316L stainless steel wire was spot-welded to each target substrate in order to allow the beam current to be measured. In order to electrically isolate the target substrate from the grounded detector housing and scattering chamber, a 13 μm thick polyethylene sheet was inserted between the substrate and the plastic scintillator and steel tube. The beam current striking the target was then read out into an ORTEC 439 current integrator. Originally, a 105 V battery stack composed of eleven standard 9 V PP3 batteries was used to positively bias the target to provide secondary electron suppression.

Unfortunately, because of the not-quite large enough resistance of the polyethylene, this resulted in a constant flow of about 20 nA, so the experiment was carried out without secondary electron suppression.

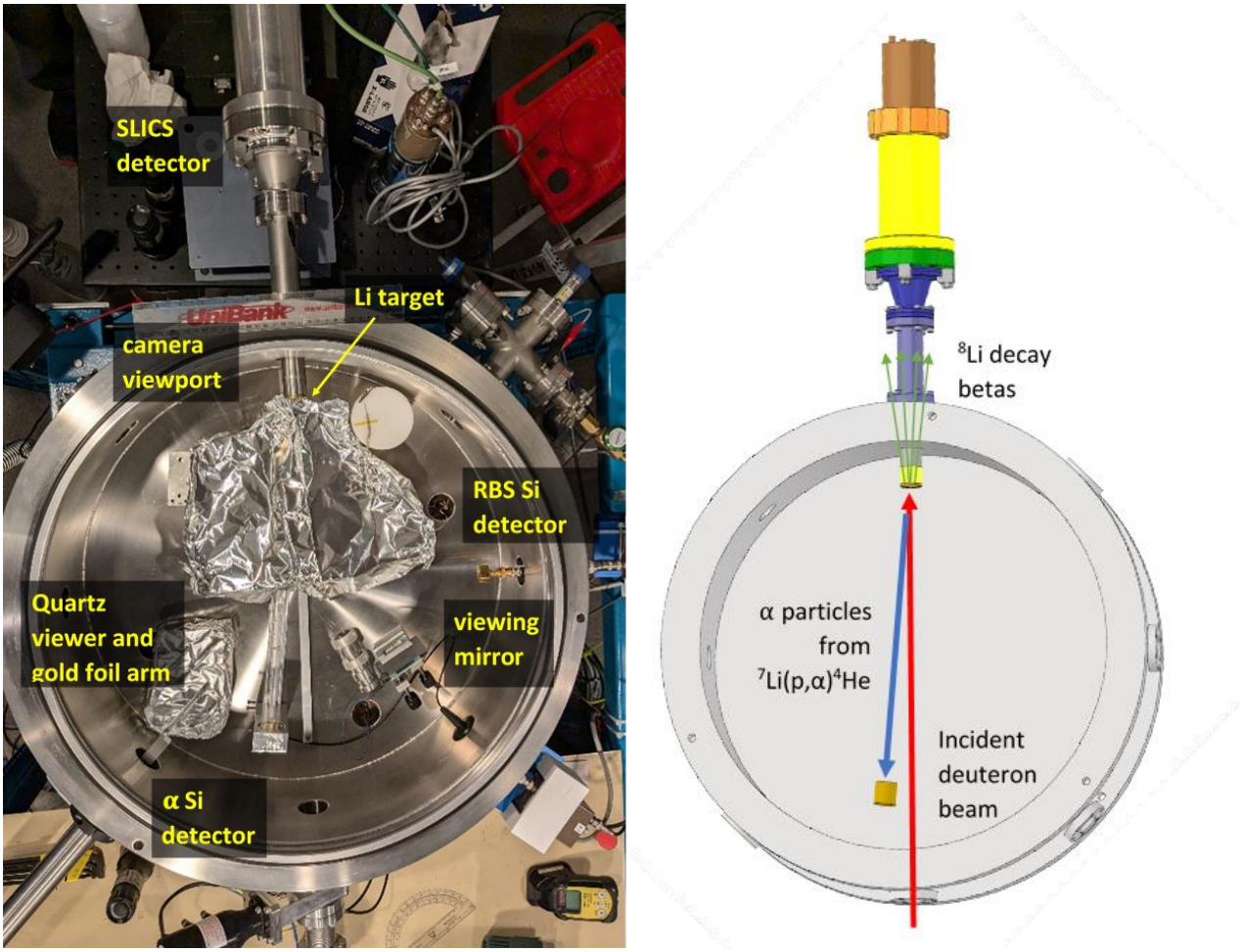

Figure 12. (Right) Top view of 30R scattering chamber showing the placement of the detectors and other components. (Left) The deuteron beam enters the chamber and strikes the lithium film on the end of the SLICS detector, which detects beta particles from the decay of ^{8}Li created by ^{7}Li(d,p)^{8}Li. Alpha particles from the ^{6}Li(d,α)^{4}He reaction scatter at 173.4° into the 500 mm^2 silicon detector.

In order to view and measure the position of the beam spot on the lithium target, a glass slide was attached to a motion feedthrough arm that allowed the slide to be raised and lowered in front of the lithium target. A mirror placed in the chamber as shown in Figure 12 allowed a camera to see the glass slide, albeit at an angle. By using the measured geometry, it was possible to reconstruct the position of the beam spot on the target from the images captured by the camera.

Figure 12 also shows another motion feedthrough which allowed a 0.116 μm thick foil of 24 carat gold (96% gold, 3.5% silver, and 0.5% copper) to be inserted into the beam at the center of the scattering chamber, upstream of the SLICS detector and lithium target, at an angle of 45°. The arm carrying the gold foil held another glass viewer that was used to position the gold foil in the beam. This glass slide could be viewed without moving the same camera, simply by changing the focus. A second silicon detector, with an active area of 100 mm^2, was placed 24.6 cm from the gold target to detect deuterons scattered elastically at an angle of 90°.

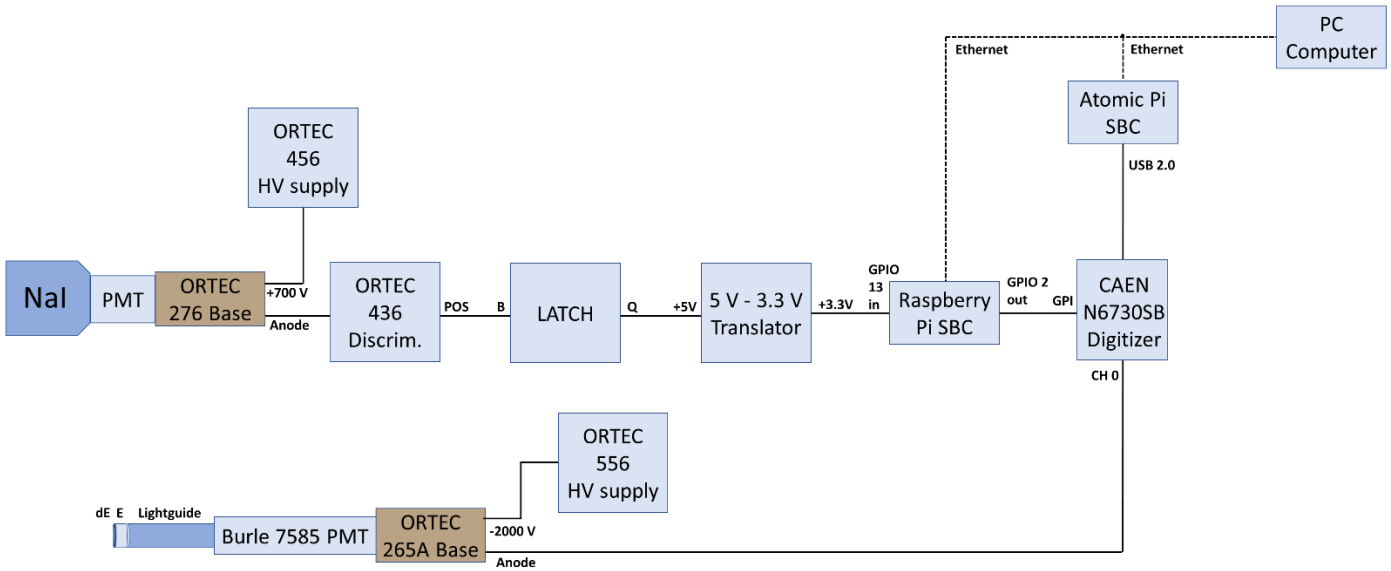

Figure 13. Block diagram of electronics. A latch circuit, which reset every time it received a pulse from the NaI detector, generated a trigger pulse for the Raspberry Pi. When the beam was stopped, if the latch was not reset in $\lesssim$ **10** ms the Raspberry Pi 4, which controlled the timing of the experiment, started the CAEN digitizer.

The procedure for the experiment was as follows. The beam spot was moved across the lithium target in steps of approximately 1 mm. At each step, a series of measurements were made to allow the absolute efficiency of the detector to be determined for each position on the target.

1. The first task at each setting was to position the beam using the quartz viewer in front of the lithium target. Since there was no collimation, the quadrupole magnets were used to produce the most compact possible beam spot, and to move it into the correct position. Usually there was a bright core spot and a faint "halo" or "tail". A typical beam spot is shown in Figure 14.

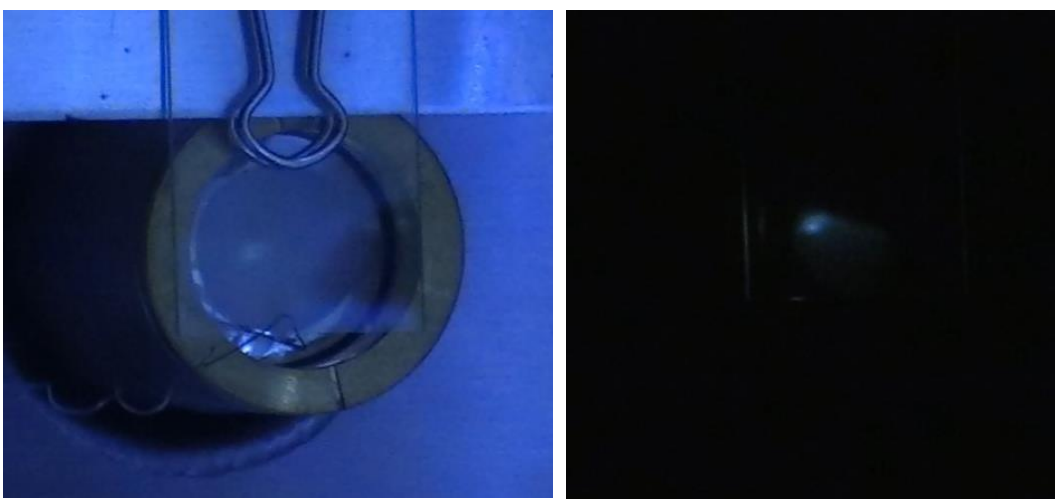

Figure 14. Typical photographs of the beam spot on the quartz viewing window with the lights on (left), showing the end of the detector, the substrate, and the lithium coating, and with the lights off (right) showing the central beam spot and a faint "tail".

2. Next, without changing the beam, the front viewer was inserted into the beam, and used to position the gold foil with the beam passing through its center. Deuterons elastically scattered at 90° from the gold foil were counted for 30 seconds to determine the beam current. This was done with the quartz

window still covering the Li target to prevent activation of the oil coating on the lithium target from $^{12}C(d,n)^{13}N$.

3. The gold foil arm was then removed, and the glass viewer in from of the lithium target was raised. The deuteron beam was allowed to strike and activate the lithium target via $^{7}Li(d,p)^{8}Li$ for 5 seconds. When the beam was cut off by inserting the faraday cup after 5 seconds, the latch circuit activated the digitizer to count beta decays for the next 30 seconds. Beta events were selected on the dE-E histogram and their timestamps were histogrammed to form the decay curve, which was then integrated to form the growth curve. A fit of Equation (4) to the growth curve allowed the total number of detected beta events, $\boldsymbol{N_0}$, to be determined.
4. The faraday cup was then removed again, and the beam allowed to strike the lithium target for approximately 290 seconds, during which time the approximately 9 MeV alpha particles from $^{6}Li(d,\alpha)^{4}He$ were counted at 173.4° by the 500 mm^2 Si detector.
5. This long period of irradiation resulted in significant ^{13}N activation, which has a half-life of 9.97 minutes, by $^{12}C(d,n)^{13}N$ occurring in the oil coating. The lithium target was allowed to cool for approximately 45 minutes to reduce the background rate back down to levels where the SLICS detector could read out without overfilling its memory buffer.

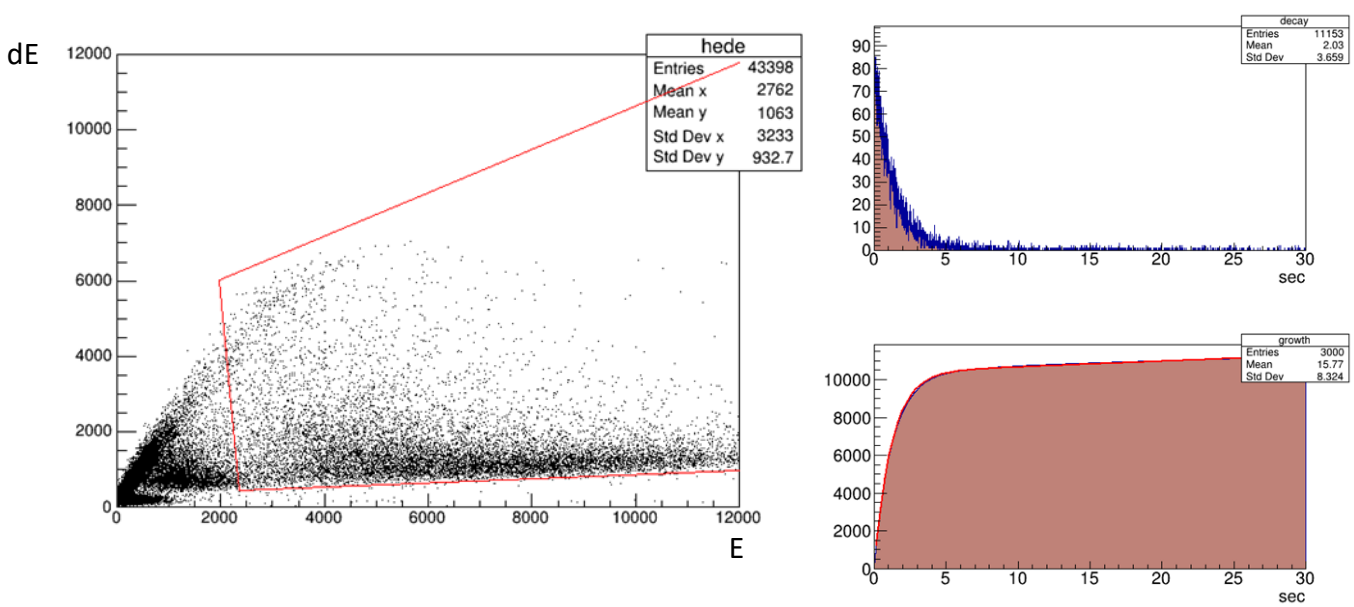

Figure 15. A typical 2D dE-E histogram (left) for counting for 30 seconds after the beam was cut off, the scale is channels. Selecting beta events inside the red polygon gives the decay curve (right top) and resulting growth curve (right bottom).

Since the intrinsic efficiency of the silicon detector is expected to be very close to 100%, the number of $^{6}Li(d,\alpha)^{4}He$ alpha particles detected, N_α,would be

$$N_\alpha = \frac{d\sigma}{d\Omega}(\theta)\, T\, f_6\, F\, d\Omega\, t \tag{6}$$

where $d\sigma/d\Omega\,(\theta)$ is the differential cross section for $^{6}Li(d,\alpha)^{4}He$ at laboratory angle θ (shown in Figure 16), T is the lithium area density, f_6 is the number fraction of ^{6}Li, F is the deuteron number current, $d\Omega$ is the solid angle of the silicon detector (sr) and t is the counting time (s).

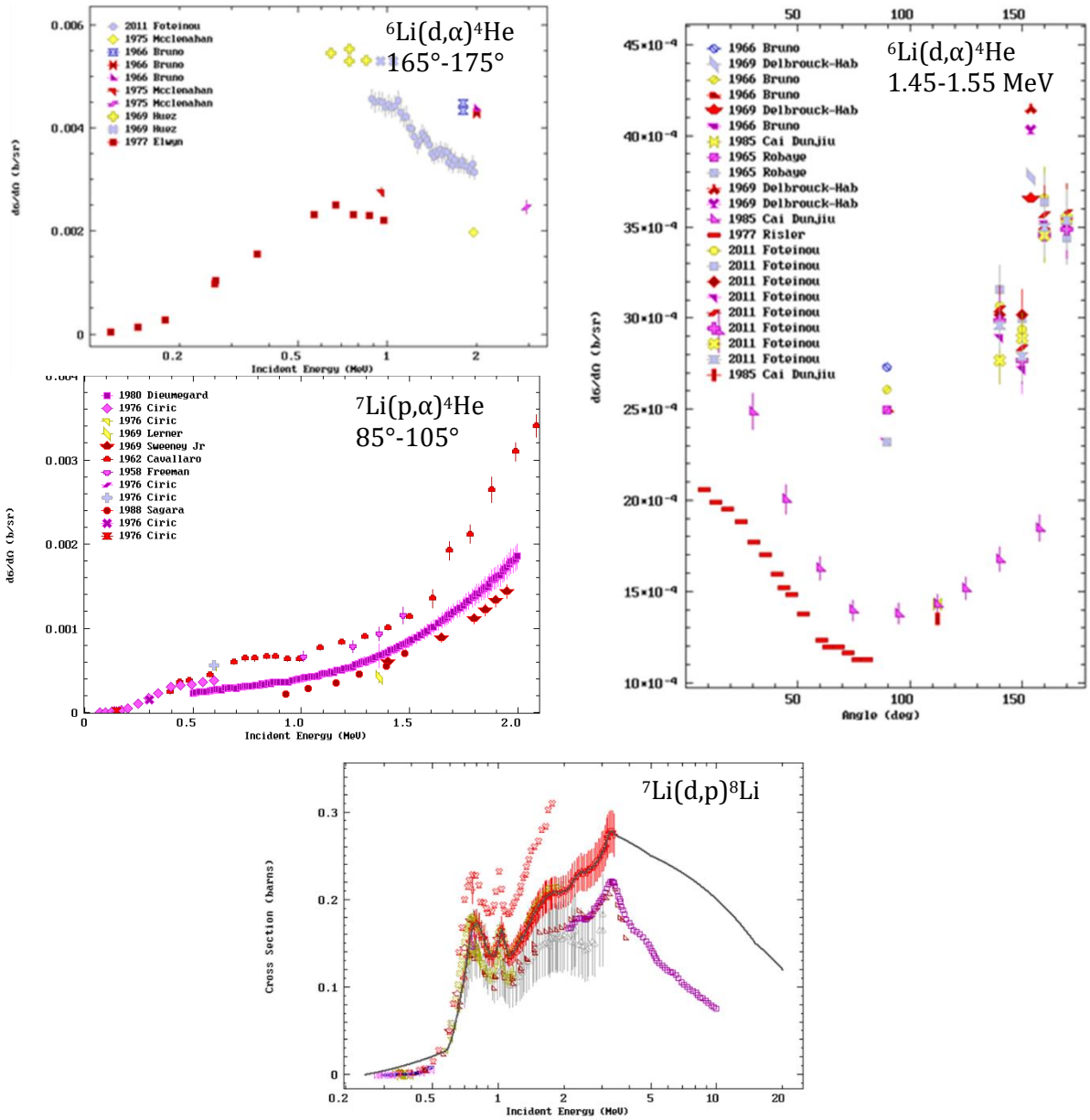

Figure 16. Differential cross section measurements for ^{6}Li(d,α)^{4}He as a function of energy for angles around 173° (top left) and as a function of angle for energies around 1.5 MeV (top right). These, as well as measurements of the differential cross section for ^{7}Li(p,α)^{4}He around 90° (middle left) used to determine lithium target thickness and the total cross section for ^{7}Li(d,p)^{8}Li as a function of energy (bottom) disagree by as much as a factor of three. The solid black line in the ^{7}Li(d,p)^{8}Li plot is the ENDF/B-VIII.0 evaluated cross section. Plots generated by EXFOR [20].

The measured value of N_α can be used to measure the current F

$$F = \frac{N_\alpha}{\frac{d\sigma}{d\Omega}(\theta)\, T\, f_6\, d\Omega\, t} \tag{7}$$

to roughly the same accuracy as the previously measured ^{6}Li(d,α)^{4}He cross section $d\sigma/d\Omega$. This measurement of the beam current, as well as the values from RBS from the gold foil and the current integrator can be used to determine the efficiency, since from Equation (2) the number of ^{8}Li product nuclei, N_{8Li}, would be

$$N_{8Li} = \frac{\sigma\, F\, T\, f_7}{\lambda} \tag{8}$$

where σ is the total cross section for ^{7}Li(d,p)^{8}Li and f_7 is the number fraction of ^{7}Li. Clearly then, the efficiency is just the ratio of the measured number of ^{8}Li decays, N_D, obtained by fitting the growth curve with Equation (4), to N_{8Li}

$$e = \frac{N_D}{N_{8Li}} = \frac{\lambda\, N_D}{\sigma\, F\, T\, f_7}. \tag{9}$$

One major problem with this method for determining the efficiency is the lack of reliable data for these cross sections. As can be seen in Figure 16, for the kinematics of interest, previous cross section measurements for ^{6}Li(d,α)^{4}He and ^{7}Li(d,p)^{8}Li vary by as much as a factor of three.

Figure 17 shows the preliminary results for this experiment, which are still being analyzed. The beam current, which was measured in three different ways (deuteron elastic scattering from gold, ^{6}Li(d,α)^{4}He and directly), is plotted as a function of the run number. For the direct measurements of the electrical current striking the target, the beam current is multiplied by a factor of 0.353 to account for the secondary electrons. This factor was determined by averaging over the ratio of the gold-foil current, which is believed to be the most accurate, to the measured direct target current. The current determined from counting the alphas from the ^{6}Li(d,α)^{4}He reaction has the most uncertainty, since it depends heavily on the ^{6}Li(d,α)^{4}He cross section and the measured target thickness, which in turn depends on the ^{7}Li(p,α)^{4}He cross section. The green circles in Figure 17 show the result from using the ^{6}Li(d,α)^{4}He cross section of Foteinou et al. [21] and a lithium target thickness of 1.025 μm, which was obtained using the cross sections from Dieumegard et al. [22].

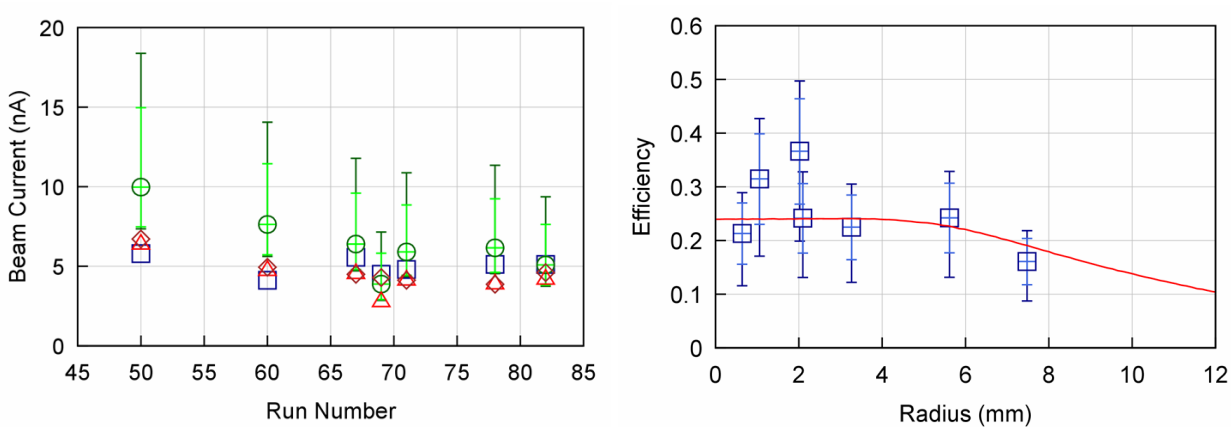

Figure 17. Preliminary results. (Left) Comparison of beam current measured using measured alphas from ^{6}Li(d,α)^{4}He (green circles), elastic deuteron scattering from gold (blue squares), and directly measuring the current striking the target substrate for 290 second runs (red triangles) and 5 seconds runs (brown diamonds). The error bars on the ^{6}Li(d,α)^{4}He measurement indicates the range in beam current resulting from the possible range of target thickness (dark green) and the possible range of the ^{6}Li(d,α)^{4}He cross section (light green). The direct current measurements were multiplied by 0.353 to account for secondary electron emission. (Right) Measured efficiency (blue squares) as a function of distance from the center of the detector using the current obtained from deuteron elastic scattering from gold, and the lithium target thickness of 1.025 μm. The error bars indicate the range in efficiency due to the range of possible target thickness (dark blue) and the range of possible ^{7}Li(d,p)^{8}Li cross sections at 1.5 MeV (light blue).

The range of $^{7}Li(p,\alpha)^{4}He$ cross sections from Figure 16 would give a possible range of lithium target thicknesses between 0.56 μm and 1.39 μm. The beam current from this range of thicknesses is shown in Figure 17 as the dark green error bar. The light green error bar shows the possible range of the current as a result of the possible range of $^{6}Li(d,\alpha)^{4}He$ cross section measurements. All of the current measurements seem be consistent with a beam current of about 5 nA.

The overall detector efficiency shown in Figure 17 was calculated using Equation (9) with the ENDF/B-VIII.0 evaluated $^{7}Li(d,p)^{8}Li$ cross section, and with the beam current obtained from deuteron elastic scattering from the gold foil and a target thickness of 1.025 μm. The dark blue error bars show the possible range of efficiency resulting from the range of target thickness from 0.56 μm to 1.39 μm, and the light blue error bar shows effect of the range of previously measured $^{7}Li(d,p)^{8}Li$ cross sections. For comparison, the red curve is the preliminary Geant4 simulation prediction for the efficiency given the dE-E selection region used in this experiment.

IV. Short-lived isotopes produced outside the OMEGA-60 target chamber (August 2024)

One possible problem with using SLICS to capture and detect short-lived radioactive nuclear reaction products formed in an ICF implosion is the high background rate in the milliseconds after the shot. During the implosion huge numbers of neutrons are released, which makes measurements of prompt radiation challenging. For example, measuring the $^{7}Li(d,p)^{8}Li$ reaction by counting the small number of prompt outgoing protons would be much harder than waiting until milliseconds after the shot, when all the neutrons are gone, and counting the ^{8}Li decays Nevertheless, the background rate may still be a problem in the milliseconds after the shot if it is elevated because of neutron activation of the target chamber and other surrounding materials. How much of a problem this presents depends on the materials used in the detector itself and the materials in the immediate vicinity of the detector. To test the ability of the SLICS detector to identify and count the reaction product decays in this radiation background field was the purpose of the OMEGA-60 ride-along experiment described below.

In December of 2019 a similar ride-along experiment [9, 10, 12] was performed using two prototype detectors and more primitive electronics than the current test. In that experiment, the two detectors –a 1-cm diameter "getter" type phoswich detector and a hollow rectangular "4π" phoswich detector – were placed on the webbing just outside the OMEGA-60 target chamber for a series of high-yield DT shots. Overall background rates were found to range up to the hundreds of thousands of events per second immediately after the shot, falling quickly with a half-life of approximately seven seconds, possibly as a result of the decay of a metastable state of ^{26}Al, created by the $^{27}Al(n,2n)^{26}Al^{*}$ reaction, which decays by positron emission with a half-life of 6.35 s, or ^{16}N produced by $^{16}O(n,p)^{16}N$ which beta decays with half-life 7.13 s. Selecting beta decay events using the 2D dE-E histogram greatly reduced this background, to the point where, for the "getter"-type detector as few as 10^{5} product nuclei per shot should be detectable.

For the planned experiment on Aug. 6, 2024, the detector developed for the 2023 MTW experiment [14, 15] and intended for use in TNSA experiments, and the "getter"-type prototype detector [11] similar to the one used in the 2019 experiment, which is intended for ICF experiments, will be placed on the webbing outside the OMEGA-60 target chamber for several high-yield DT cryogenic ICF shots. The two detectors are very similar in function, but the prototype ICF detector is of makeshift construction and has a light guide diameter of only 10 mm. The smaller diameter would be needed for a future ICF experiment to get the phoswich as close as possible to the target center without interfering with the lasers. Since

gamma background count rate goes as detector volume, this will allow the solid angle for capturing product nuclei to be large while minimizing gamma background. For the TNSA detector, the diameter was selected to allow the phoswich to be far enough away to use TOF on the incident ions, while maintaining adequate solid angle.

Table 2. Detectors to be tested in the OMEGA-60 ride-along experiment.

Detector	ICF detector	TNSA detector
		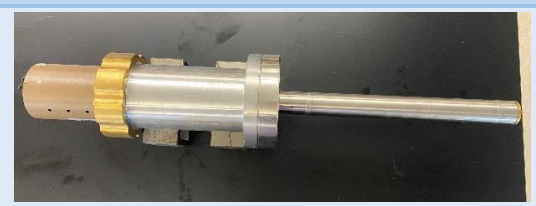
Previous use	2019 OMEGA-60 ride-along prototype "getter" type	2023 MTW TNSA experiment
Phoswich/ Lightguide Diameter	10 mm	25.4 mm (1")
Phoswich/ Lightguide Length	305 mm (12")	308 mm
Lightguide material	clad borosilicate glass, NA 0.66	unclad Schott F2 glass

Figure 18 shows the design of the support stand that will be used to hold the detectors in position on the webbing outside the OMEGA-60 target chamber. The support rail is constructed of 6061 aluminum, with 3D printed PLA plastic sliders that hold the detectors. The sliders will be fixed in place by set screws on the side of the rail, and the detectors are held to the sliders with steel hose clamp bands.

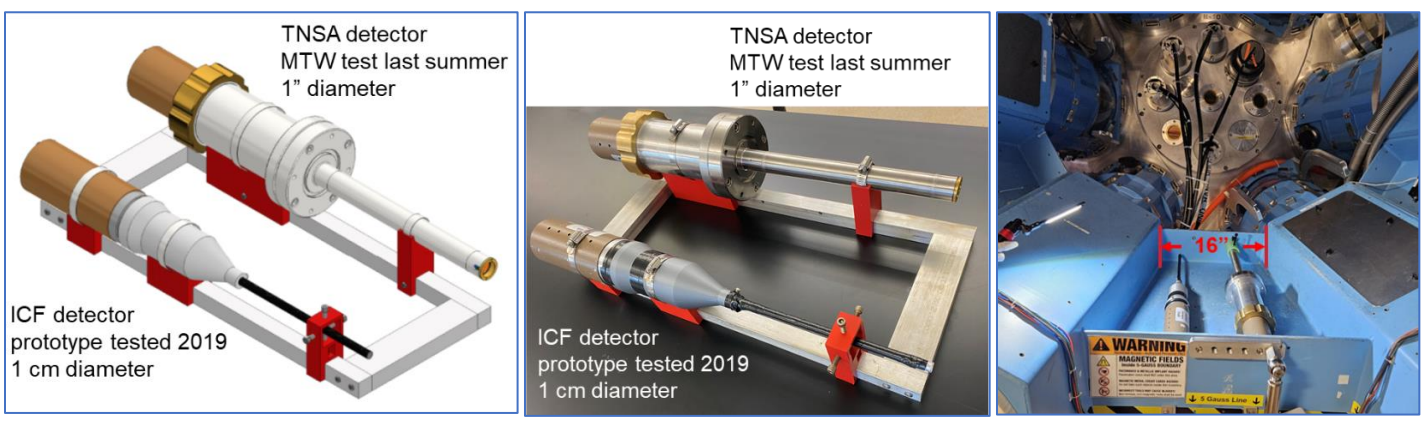

Figure 18. CAD drawing (left) and photograph (center) of the detector support structure. Photograph (right) shows what the detectors will look like in the OMEGA-60 webbing.

A block diagram of the electronics, which are similar to the setup used for the MTW experiment [14] in 2023, is shown in Figure 19. A 400 ns TTL trigger signal from HTS LaCave(B) crate will be lengthened to about 5 μs in order to be used as the logic signal input to the Raspberry Pi 4 which will control the timing of the experiment. When a shot trigger was detected, the Raspberry Pi will wait for 1 ms, then connect both the high voltage (HV) and HV ground to the detector using the MOSFET electronic relay circuit shown in Figure 20 to activate 15 kV high-voltage isolation reed relays. At 2 ms after the shot, another

set of relays will connect the signal and signal ground. The relays are to prevent any voltage spike caused by the electromagnetic pulse (EMP) from damaging the HV power supply or CAEN digitizer. At about 4 ms after the shot, the Raspberry Pi 4 will send a signal to the CAEN digitizer to begin data collection. In this way for data collection will begin within a few ms after the laser shot.

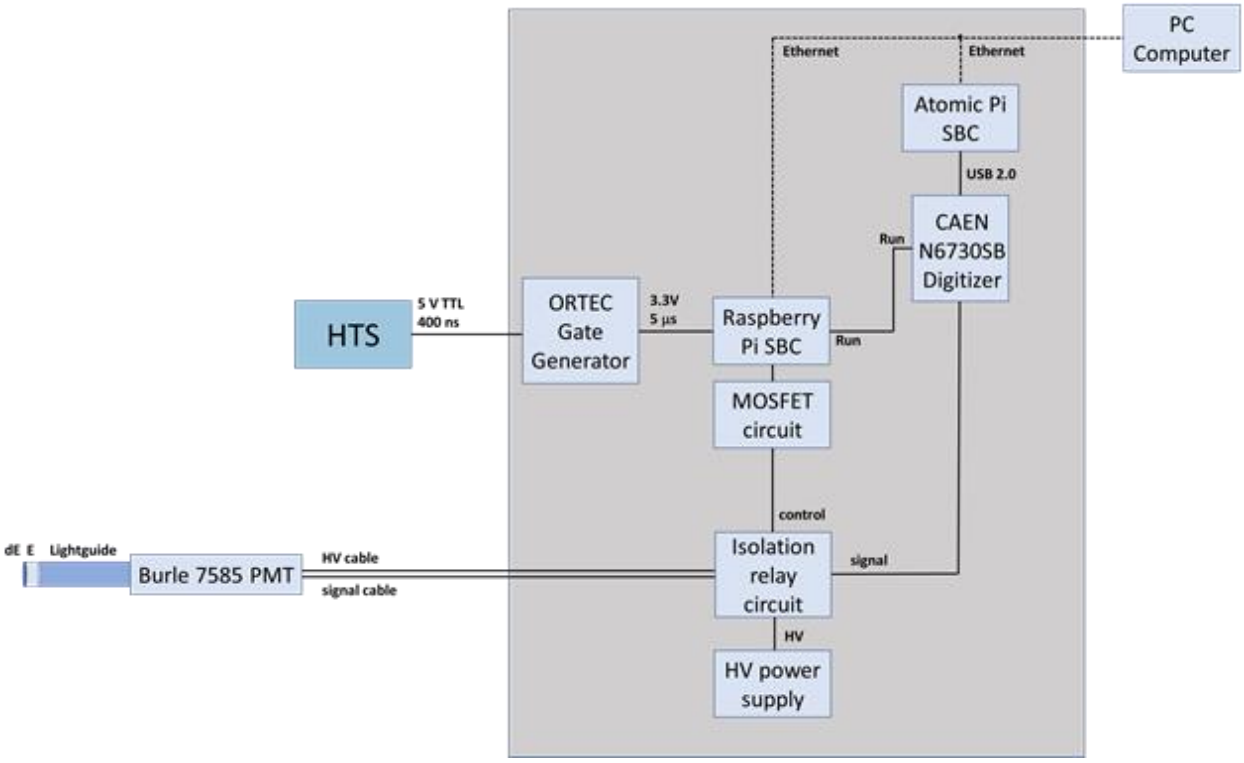

Figure 19. Electronics setup. Prior to the laser shot, the detector will be electrically isolated from the detector. A TTL control signal indicating the timing of the laser shot will trigger the Raspberry Pi 4 single board computer, which controls the experiment. It will wait for about 1 ms before turning on the MOSFET switches which close the high-voltage isolation relays connecting the high voltage, signal, and ground to the detector. About 2 ms later, the Raspberry Pi will signal the CAEN digitizer to begin collecting data, which is rapidly read out into the Atomic Pi single board computer.

The objectives for this experiment, which will be carried out as a ride-along experiment to a set of high-yield cryogen DT shots under the Cryo_FlashFreeze_ReturnShock-24A campaign, are to test the ability of the SLICS system to switch on HV and start counting after the initial burst of photons, electrons, protons, and neutrons and to study background rates and dE-E distributions from ~4 ms to 20 s after the shot. A secondary objective will be to simulate the requirements of an actual ICF activation experiment – namely, to determine whether, in the extreme radiation environment after a high yield shot, radioactive product nuclei can be detected.

To do this, two 25.4 mm (1 inch) diameter, 100 µm thick boron carbide discs will be placed in front of the TNSA detector and secured under the brass retaining ring, as shown in Figure 21, in the same way as the lithium targets from the 2023 MTW experiment. The 14.1 MeV primary DT neutrons produced in the implosion will activate the boron to produce ^{8}Li via the ^{11}B(n,α)^{8}Li reaction. An attempt will be made to identify the ^{8}Li beta decay events using the 2D dE-E histogram, and then fit the decay of these events to confirm they are from ^{8}Li. If this can be done, then the total number of ^{8}Li can be measured assuming the detector efficiency is known (see previous section). A back of the envelope estimate for the number of ^{8}Li nuclei expected to be produced is about 50,000 – a number similar to the expected yield in an ICF activation-type experiment.

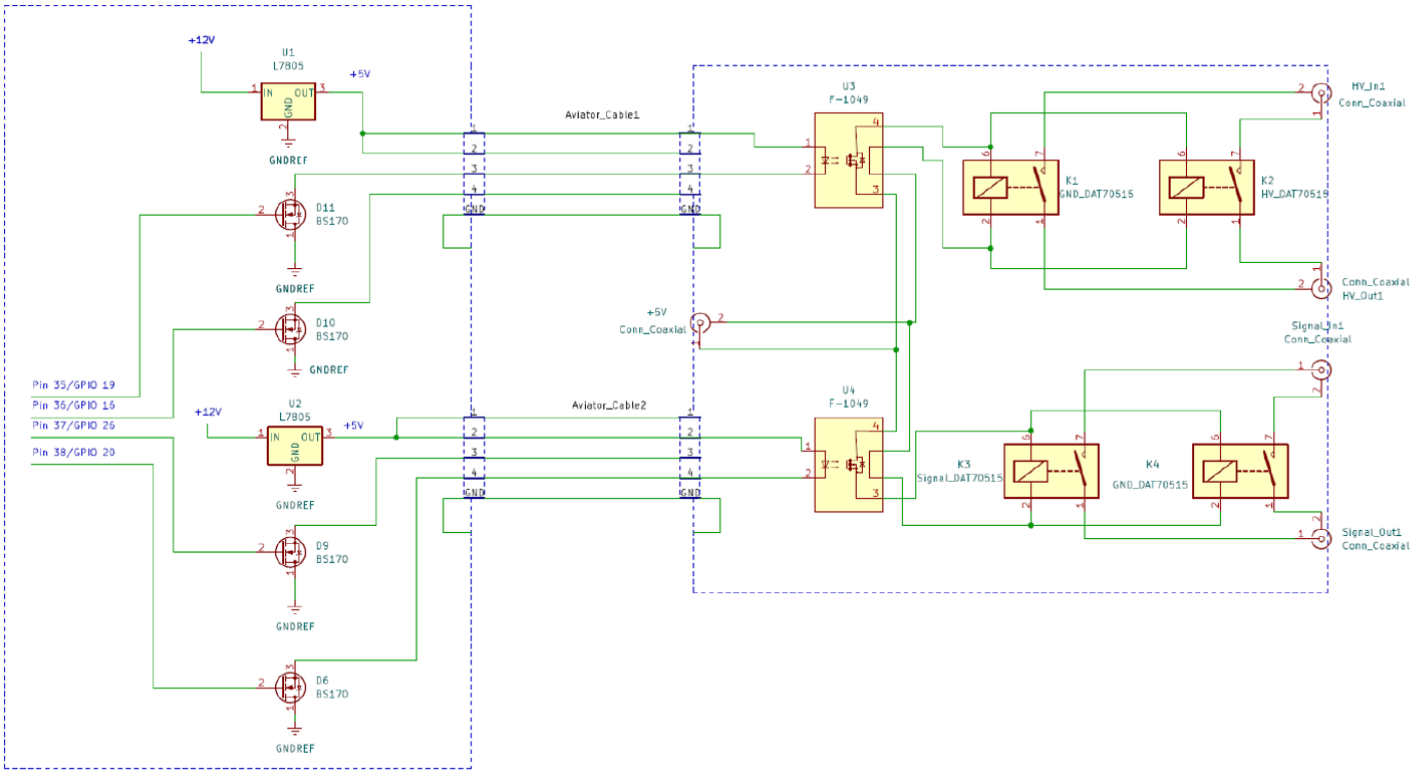

Figure 20. MOSFET circuit schematic. The Raspberry Pi GPIO switch MOSFETs which in turn power MOSFET solid state relays. These then switch the high speed isolation relays that isolate the HV, signal, and ground for the PMT.

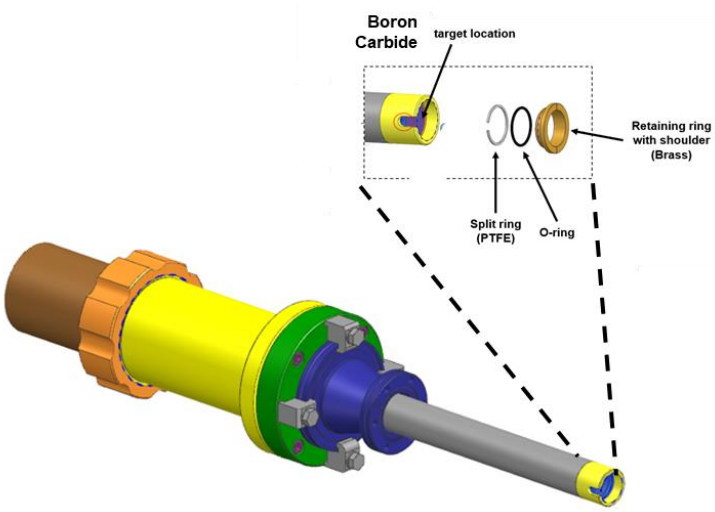

Figure 21. Boron carbide discs will be placed under the retaining ring on the TNSA detector, in the place where the nuclear target would normally reside. Primary DT neutrons from the ICF implosion will create 8Li in the boron discs via the $^{11}B(n,\alpha)^{8}Li$ reaction.

V. Future Plans

In the next few months work will begin on a design to insert the TNSA detector used in the 2023 MTW experiment into a Ten-Inch Manipulator (TIM) for use in the OMEGA-EP or OMEGA-60 target chambers. This will allow it to be used for TNSA driven activation experiments using tritium and to make use of the higher ion energies made possible with the OMEGA-EP rather than MTW lasers. By replacing the 25.4 mm (1 inch) diameter phoswich detector and light guide with a smaller diameter, similar to the prototype detector in Figure 18, the SLICS system could also be used for ICF measurements.

This detector system would be a natural precursor for more advanced detectors of this type that could be used with the proposed NSF OPAL platform to improve the measurement of total reaction cross sections of tritium-lithium and tritium-beryllium reactions. By using SLICS as an activation diagnostic in combination with the high shot rate possible with NSF OPAL, numerous light-ion induced reactions could be studied, with relevance to nucleosynthesis models and structure of neutron-rich nuclei.

VI. Talks given since summer 2023

Chunsun Lei and Mark Yuly**, "Deposition System for Thin Lithium Nuclear Targets,"** XLII Annual Rochester Symposium for Physics Students, University of Rochester, April 20, 2024. (https://dspace.houghton.edu/handle/hc/4181)

Andrew Martin and Mark Yuly**, "Target Normal Sheath Acceleration as a Technique for Measuring Nuclear Cross-Sections,"** XLII Annual Rochester Symposium for Physics Students, University of Rochester, April 20, 2024. (https://dspace.houghton.edu/handle/hc/4183)

VII. Posters presented since summer 2023

Chunsun Lei, Noah Harley, Andrew Hotchkiss, Andrew Martin, Mark Yuly, Stephen J. Padalino, Chad J. Forrest, Thomas C. Sangster, Sean P. Regan, **"A TNSA Technique to Measure Light-Ion Cross Sections Using the MTW Laser,"** 15th OMEGA Laser User's Group Meeting, Laboratory for Laser Energetics, Rochester, NY, April 17, 2024; XLII Annual Rochester Symposium for Physics Students, University of Rochester, April 20, 2024; 65th Annual Meeting of the APS Division of Plasma Physics, Denver, CO, October 30 – November 3, 2023. (https://dspace.houghton.edu/handle/hc/4144)

Chunsun Lei, Noah Harley, Andrew Hotchkiss, Andrew Martin, Mark Yuly, Stephen J. Padalino, Chad J. Forrest, Thomas C. Sangster, Sean P. Regan, **"Coated Li Film Targets for TNSA Light-Ion Reaction Experiments with the MTW Laser,"** 15th OMEGA Laser User's Group Meeting, Laboratory for Laser Energetics, Rochester, NY, April 17, 2024; XLII Annual Rochester Symposium for Physics Students, University of Rochester, April 20, 2024; 65th Annual Meeting of the APS Division of Plasma Physics, Denver, CO, October 30 – November 3, 2023. (https://dspace.houghton.edu/handle/hc/4143)

This material is based upon work supported by the Department of Energy [National Nuclear Security Administration] University of Rochester "National Inertial Confinement Program" under Award Number(s) DE-NA0004144.

---

[1] H. Abu-Shawareb et al., Phys. Rev. Lett. **129**, 075001 (2022).

[2] A. B. Zylstra et al., Nature **601**, 542–548 (2022).

[3] H. Abu-Shawareb et al., Phys. Rev. Lett. **132**, 065102 (2024).

[4] A.K. Schwemmlein, C. Stoeckl, C.J. Forrest, W.T. Shmayda, S.P. Regan, W. U. Schröder, NIM B **522**, 27 (2022).

[5] Katelyn Cook, B.S. thesis, (Houghton College, 2019).

[6] Mark Yuly, Stephen Padalino, Micah Coates and Katelyn Cook, "A possible measurement of the 3H(t,γ)6He cross section at low energy," in Nuclear and Plasma Diagnostics for the EP-OMEGA and MTW Laser Systems, LLE Proposal for Subaward 416231-G, 2016 (unpublished).

[7] Mark Yuly, Stephen Padalino, Micah Coates and Katelyn Cook, "A Phoswich Detector System to Measure the $^{3}H(t,\alpha)^{6}He$ Cross Section using ICF" in Nuclear and Plasma Diagnostics for the EP-OMEGA and MTW Laser Systems, LLE Proposal for Subaward 416231-G, 2017 (unpublished).

[8] Mark Yuly, Stephen Padalino, Emma Bruce, Katelyn Cook, and Sarah Hull, "Measuring Low Energy Nuclear Cross Sections using ICF," in Nuclear and Plasma Diagnostics for the EP-OMEGA and MTW Laser Systems, LLE Proposal for Subaward 416231-G, 2018 (unpublished).

[9] Mark Yuly, Stephen Padalino, Tyler Kowalewski, Salvatore Ferri and Steven Raymond, "Inertial Confinement Fusion as a Tool to Study Fundamental Nuclear Science," in Nuclear and Plasma Diagnostics for the EP-OMEGA and MTW Laser Systems, LLE Proposal for Subaward 416231-G, 2019 (unpublished).

[10] Mark Yuly, Stephen Padalino, Micah Christensen, Joshua Bowman, "Progress toward using ICF to measure light-ion nuclear cross sections" in Nuclear and Plasma Diagnostics for the EP-OMEGA and MTW Laser Systems, LLE Proposal for Subaward 416231-G, 2020 (unpublished).

[11] Mark Yuly, Stephen Padalino, Adam Brown, Micah Christensen, Micah Condie, "Trapping and detecting trace radioactive isotopes produced in ICF implosions," in Nuclear and Plasma Diagnostics for the EP-OMEGA and MTW Laser Systems, LLE Proposal for Subaward 416231-G, 2021 (unpublished).

[12] Tyler Kowalewski, "Inertial Confinement Fusion as a Tool to Study Fundamental Nuclear Science," B.S. Thesis (Houghton College, 2021).

[13] Mark Yuly, Stephen Padalino, Adam Brown, Andrew Hotchkiss, Chunsun Lei, Andrew Martin. "Trapping and detecting trace radioactive isotopes produced in ICF implosions," in Nuclear and Plasma Diagnostics for the EP-OMEGA and MTW Laser Systems, LLE Proposal for Subaward 416231-G, 2022 (unpublished).

[14] Mark Yuly, Stephen Padalino, Noah Harley, Andrew Hotchkiss, Chunsun Lei, Andrew Martin. "A new technique for measuring light ion nuclear reactions using TNSA," in Nuclear and Plasma Diagnostics for the EP-OMEGA and MTW Laser Systems, LLE Proposal for Subaward 416231-G, 2023 (unpublished).

[15] Andrew Martin, B.S. thesis, (Houghton College, 2023).

[16] Chunsun Lei, B.S. thesis, (Houghton College, 2023).

[17] M. Bikchurina et al., Proceedings of ISINN-29, JINR, E3-2023-58, Dubna, 2023, p.75 – 87

[18] A. Schwemmlein, Ph. D. thesis, (University of Rochester, 2021).

[19] G. Soti, F. Wauters, M. Breitenfeldt, P. Finlay, I.S. Kraev, A. Knecht, T. Porobić, D. Zákoucký, and N. Severijns, NIM A **728**, 11-22 (2013).

[20] N. Otuka, et al., Nuclear Data Sheets 120, 272-276 (2014).

[21] V. Foteinou et al., NIM B **269**, 2990 (2011).

[22] D. Dieumegard et al., NIM **168**, 93 (1980).